THE ASTROPHYSICAL JOURNAL, 375:583–593, 1991 July 10

IMAGING SPECTROPHOTOMETRY OF IONIZED GAS IN NGC 1068. III. ANISOTROPIC EXCITATION OF THE LARGE-SCALE DISK BY SCATTERING OF NUCLEAR CONTINUUM

JAMES SOKOLOWSKI AND JONATHAN BLAND-HAWTHORN
Department of Space Physics and Astronomy, Rice University, Houston, TX 77251-1892

AND

GERALD CECIL
Department of Physics and Astronomy, University of North Carolina, Chapel Hill, NC 27514
Received 1990 August 27; accepted 1991 January 4

ABSTRACT

Imaging Fabry-Perot spectrophotometry has revealed a diffuse ionized medium (DIM) pervading the inner 10 kpc of the disk of NGC 1068. These data show that the DIM has high [N II] λ6584/Hα emission-line ratios (from 0.6 to 1.3) over much of the disk, with even higher ratios (from 1.3 to 2.5) near the nucleus and in isolated regions near the radio jet axis. Previous studies find that other low-excitation emission, such as [O II] λ3727 and [S II] $\lambda\lambda$6716, 6731, is also high away from the jet axis, while high-excitation emission such as [Ne V] $\lambda\lambda$3346, 3426 and He II λ4686 is found only within two diametric sectors of opening angle $\sim 80°$, aligned along the axis. We show that these emission characteristics can be understood in the light of the developing picture of NGC 1068, in which its intrinsic type 1 Seyfert nucleus, concealed by an obscuring medium, is visible only through scattered, polarized light. In this picture the gas excitation is anisotropic, the high-excitation gas along the jet axis being photoionized by direct nuclear continuum, while the lower excitation gas away from the axis sees only indirect nuclear emission scattered into it. We consider in detail, a model of low optical depth ($\tau_S = 0.1$), near-nuclear Thomson scattering and show that even with moderate dust extinction ($E \leq 0.3$ mag kpc^{-1}), this mechanism is sufficient to energize the DIM. This model provides ionization parameters that produce both globally enhanced, low-ionization lines such as [N II] λ6584, [O II] λ3727, and [S II] $\lambda\lambda$6716, 6731 and high-excitation emission such as [Ne V] $\lambda\lambda$3346, 3426 and He II λ4686 confined to the two diametric sectors along the radio axis. These Fabry-Perot data require a flux of ionizing photons far larger than those produced by dust-scattering models using standard grain compositions and size distributions. We therefore favor electrons as the dominant source of scattering of the nuclear ionizing radiation.

Subject headings: galaxies: individual (NGC 1068) — galaxies: interstellar matter — galaxies: Seyfert — interferometry — spectrophotometry

1. INTRODUCTION

Regions of extended line emission, which we term diffuse ionized media (DIM), are found in many galactic environments. Baum & Heckman (1989) detect extended optical emission, aligned along radio jet axes, from their entire sample of 38 powerful radio galaxies ($L_x \geq 5 \times 10^{41}$ ergs s^{-1}), with extent and power well correlated with core radio power and spectral shape. Spinrad & Djorgovski (1984) detect extended optical emission along radio jet axes from half of their sample of 13 high-redshift radio galaxies. In a sample of 20 Seyfert galaxies, surveys by Unger et al. (1987) and Wilson, Ward, & Haniff (1988) find extended optical emission-line gas aligned with known radio jets. Robinson et al. (1987) show that the regions of extended optical emission detected in external galaxies form a smooth locus of points on standard line ratio plots, best explained by power-law photoionization, while Wilson et al. (1988) show that shock excitation models yield poor fits to the observed emission line intensities.

NGC 1068 is the closest, luminous Seyfert 2 galaxy (14.1 Mpc; Tully 1988) and contains a wealth of interesting activity. The inner 1 kpc displays a bipolar radio jet (Wilson & Ulvestad 1983), a stellar bar most prominent in the IR (Thronson et al. 1989), but also seen in detailed Fabry-Perot optical velocity maps (Bland-Hawthorn et al. 1991), bipolar cones of high-excitation gas (Bergeron, Petitjean, & Durret 1989; Pogge 1988) as well as an elliptical ring of starburst activity (Scoville, Young, & Lucy 1983; Myers & Scoville 1987). These central phenomena are well aligned along position angle $\sim 45°$, suggesting some connection. Recent spectropolarimetry work (Antonucci & Miller 1985; Bailey et al. 1988) shows that inside the Seyfert 2 nucleus of NGC 1068 there exists a hidden broad line region. In the currently emerging picture, the "type 1" nature of this nucleus is hidden by a geometrically and optically thick absorbing medium distributed anisotropically. The simplest adequate geometry for this medium is that of a torus. The detection of the Seyfert 1 spectrum in NGC 1068 is due to the scattering of nuclear flux, initially directed out through the polar openings of the obscuring torus, into our line of sight, from a region located within a few arcseconds of the nucleus. Antonucci & Miller (1985) find no evidence for wavelength dependence in the scattered flux, suggesting that Thomson scattering is responsible, although they cannot rule out scattering by dust with an anomalous size distribution (Bohlin & Savage 1981). The detection of Fe Kα nuclear emission at 6.5 keV and the detection of nuclear power-law continuum out to 15 keV, with spectral index $\alpha \simeq -0.55$ (Koyama et al. 1989), would also suggest that Thomson scattering is predominant in the nucleus. Bailey et al. (1988), detecting significant wavelength structure in their polarized spectra, favor a dust scattering mechanism although are unable to rule out a substantial

component of Thomson scattering. The degree of optical polarization suggests that the scattering optical depth τ_S is $0.04 \leq \tau_S \leq 0.1$ (Antonucci & Miller 1985; Krolik & Begelman 1986).

Extended line emission has been detected in NGC 1068. By forming the ratio of [O III] $\lambda\lambda$4959, 5007 to [N II] $\lambda\lambda$6584, 6548 + Hα filter images, Pogge (1988) finds two sectors of high-excitation emission along the jet axis. A number of spectroscopic studies (Nishimura, Kaneko, & Toyama 1984; Baldwin, Wilson, & Whittle 1987; and Bergeron et al. 1989) detect high-excitation [Ne V] $\lambda\lambda$3346, 3426 and He II λ4686 emission also along the jet axis. Away from the jet axis, Evans & Dopita (1987, hereafter ED87) detect a high-excitation component superposed upon their spectra of 13 H II regions. They concluded that the N/O and S/O abundance ratios were solar while the O/H ratio was approximately solar, being enhanced by no more than 30%. Diagnostic line ratio plots have shown that photoionization is the preferred ionization mechanism for high excitation gas in NGC 1068 (Nishimura et al. 1984; ED87; Bergeron et al. 1989).

Recent imaging Fabry-Perot spectrophotometry (Bland-Hawthorn, Sokolowski, & Cecil 1991, hereafter Paper II) reveals the full extent and detailed morphology of the DIM in NGC 1068. These data show that the DIM surface brightness declines as $\simeq r^{-2}$ away fom the nucleus and has deprojected elliptical isophotes ($e \sim 0.5$) along P.A. $\sim 45°$. The DIM is detected out to radii of 5.3 kpc and 3.8 kpc from the nucleus, parallel and perpendicular to the jet axis respectively. Regions of highest [N II] λ6584/Hα ratio and most intense emission are seen in two sectors spatially coincident with the regions of high excitation detected by previous authors. These data and the developing picture of the nuclear structure are highly suggestive of an underlying connection between the hidden Seyfert 1 nucleus and the morphology and emission properties of the DIM. In this picture, the gas excitation is anisotropic: regions that see the nucleus directly have highest excitation, while regions that see only scattered nuclear flux have lower excitation.

This paper considers photoionization of the solar abundance DIM in NGC 1068 by anisotropic nuclear emission. A review of the basic obscuration picture is found in § 2. A model for the global excitation of the DIM in NGC 1068 by direct and scattered nuclear continuum is examined in detail in § 3, where model constraints are obtained from small-aperture spectropolarimetry. Here the energetics, ionization state, emission properties, and geometry of the DIM are discussed and relevant scattering mechanisms are examined. Photoionization modelling of emission from the DIM of NGC 1068 is discussed in § 4. Concluding remarks are given in § 5.

2. THE OBSCURING TORUS PARADIGM

An obscuring torus is characterized by the amount of solid angle (denoted $4\pi - \Delta\Omega$) it subtends as seen from its center, the galaxy nucleus. Only lines of sight along the polar openings, within the solid angle $\Delta\Omega$, can extend from the nucleus out to infinity. For a nuclear continuum source of intrinsic luminosity L_I, a fraction of this luminosity, $(1 - \Delta\Omega/4\pi)L_I$ is absorbed by the obscuring medium and presumably reradiated in the infrared, while only $(\Delta\Omega/4\pi)L_I$ emerges from the obscuring torus. From the ratio of type 1 to type 2 Seyferts in IR-bright galaxy samples (de Grijp et al. 1985; Osterbrock & DeRobertis 1985), it is found that $\Delta\Omega/4\pi \sim \frac{1}{4}$ (Krolik & Begelman 1986). Modeling of the nuclear outflow in NGC 1068 (Cecil, Bland, & Tully 1990, hereafter Paper I) shows that the opening angle of the torus is $\sim 80°$ which is in accord with this observed ratio. We will refer to the cones defined by the open solid angle, $\Delta\Omega$, as the direct cones, because material in them sees the active nucleus directly.

In the context of an obscuring torus model, the relative orientation between a particular Seyfert galaxy's torus and the observer determines the classification of that galaxy. The properties of a Seyfert 1 galaxy arise from a direct view of the active nucleus, while for a Seyfert 2, the obscuring torus blocks the nuclear regions from sight. This picture requires that the symmetry axis of the torus be decoupled dynamically from the galaxy disk axis due to the lack of correlation between the inclination of Seyfert disks and Seyfert type (Wilson & Heckman 1985). This is supported in the case of NGC 1068 by the derived geometry of its nuclear outflow (Paper I) which shows that the torus symmetry axis is inclined to the galaxy disk by $\sim 45°$. The detection of the BLR and the nuclear continuum source in polarized light is due to near-nuclear scattering, into our line of sight, of the hidden emission from the direct cones.

The current state of the spectropolarimetric observations is incapable of determining the exact nature of the near-nuclear scattering mechanism. The observations of Antonucci & Miller (1985) favor wavelength-independent Thomson scattering, while those of Bailey et al. (1988) indicate that dust scattering predominates. Neither set of observations can determine the relative importance of extranuclear scattering, although the high dust content of the inner disk of NGC 1068 suggests that this component could be significant. We will assume that Thomson scattering dominates the scattering of ionizing continuum in the nuclear regions of NGC 1068 because as we show in § 3 below, standard dust mixtures (Mathis, Rumpl, & Nordsieck 1977, hereafter MRN) are incapable of scattering sufficient ionizing photons to power the DIM away from the direct cones. Thus with the measured (i.e., scattered) nuclear spectrum, and adopted values for the torus opening angle and scattering optical depth, we can fully determine the strength of the direct nuclear continuum. Of that fraction of the intrinsic nuclear luminosity that escapes the torus, $e^{-\tau_S}(\Delta\Omega/4\pi)L_I$ propagates out into the direct cones while $(1 - e^{-\tau_S})(\Delta\Omega/4\pi)L_I$ is scattered into the rest of the disk.

For later convenience in calculating ionization parameters and Strömgren radii, we choose to parameterize the direct and scattered radiation fields by the luminosities of isotropic nuclear sources, which provide the specific intensities found in these components. We therefore write

$$L_D = e^{-\tau_S} L_I$$

$$L_S = \frac{1 - e^{-\tau_S}}{4\pi/\Delta\Omega - 1} L_I \quad (\text{for: } 0 < \Delta\Omega < 4\pi)$$

for the direct (L_D) and scattered (L_S) luminosities. In the above formulae the exponential factors determine the relative numbers of scattered photons while the geometrical factor accounts for differences in the illuminated solid angles of the direct and scattered components. Since the scattering medium is thought to be optically thin, and $4\pi/\Delta\Omega > 2$, the ratio of the direct to scattered luminosities, $(4\pi/\Delta\Omega - 1)/(e^{\tau_S} - 1)$ is greater than unity. This implies that the ionization parameters, and hence excitation conditions, to be found in the DIM inside the direct cones will be higher than those outside the cones. For $\Delta\Omega/4\pi \sim \frac{1}{4}$ and $\tau_S \simeq 0.1$ this ratio is $\simeq 30$, leading to a charac-

teristic morphological signature and a gas mass in the scattering region of less than $4 \times 10^5 M_\odot$ for realistic geometries.

3. THE DIFFUSE IONIZED MEDIUM OF NGC 1068

3.1. *Observed Properties*

Imaging Fabry-Perot spectrophotometry (Paper II) details the [N II] λ6584 and Hα flux distributions of the DIM in NGC 1068. Figure 1 reproduces the [N II] λ6584/Hα ratio map in Paper II in which values from 0.3 to 2.5 are seen. The deprojected [N II] λ6584 and Hα isophotes are elliptical ($e \sim 0.5$) and decrease radially as $\simeq r^{-2}$, becoming undetectable at radii of 5.3 kpc and 3.8 kpc along and perpendicular to the jet axis respectively (Paper II). Because the surface brightness of the DIM is significantly less than that of typical H II regions in the same data, the [N II] λ6584/Hα ratios range from 0.3 to 0.8 on the starburst ring and on isolated disk H II regions, while values of 0.6 to 1.3 are typically found elsewhere. Emission with the highest [N II] λ6584/Hα ratio is found within 10″ of the nucleus, and in two crescents, located just beyond the starburst ring, inside two diametric sectors of opening angle $\simeq 80°$ and axis position angle $\simeq 45°$, where values are 1.3–2.5. DIM emission line profiles have widths $\simeq 150$–250 km s^{-1} FWHM as compared with the line widths within the H II regions which are $\simeq 50$–150 km s^{-1} FWHM. In Paper II we interpret this as evidence for a distended distribution of the DIM gas with a scale height of at least 400 pc.

From the X-ray data of Monier & Halpern (1987) and Koyama et al. (1989), we have adopted a best-fit, three-component power law for the observed spectrum of NGC 1068. The parameters of this spectrum are given in Table 1, where L_0 is the monochromatic luminosity at 13.6 eV. There is no evidence for temporal variability in the X-ray continuum: *EXOSAT* data taken in 1983 and 1985 (Elvis & Lawrence 1988) and *Ginga* data from 1987 (Koyama et al.) contain the same flux in the 2–10 keV energy band and derive spectral indices of $\alpha_E = -0.62 \pm 0.25$ and $\alpha_E = -0.50 \pm 0.05$, respectively. There is no detection of the continuum beyond 15 keV at *Ginga*'s sensitivity.

We emphasize that for NGC 1068, an observed Seyfert 2

TABLE 1

COMPOSITE NUCLEAR CONTINUUM

Energy Range	Spectral Index	L_0 (ergs s^{-1} Hz^{-1})
13.6–100 eV	−1.55	3.8×10^{26}
100–1100 eV	−2.0	9.2×10^{26}
1100–15 keV	−0.5	1.3×10^{24}

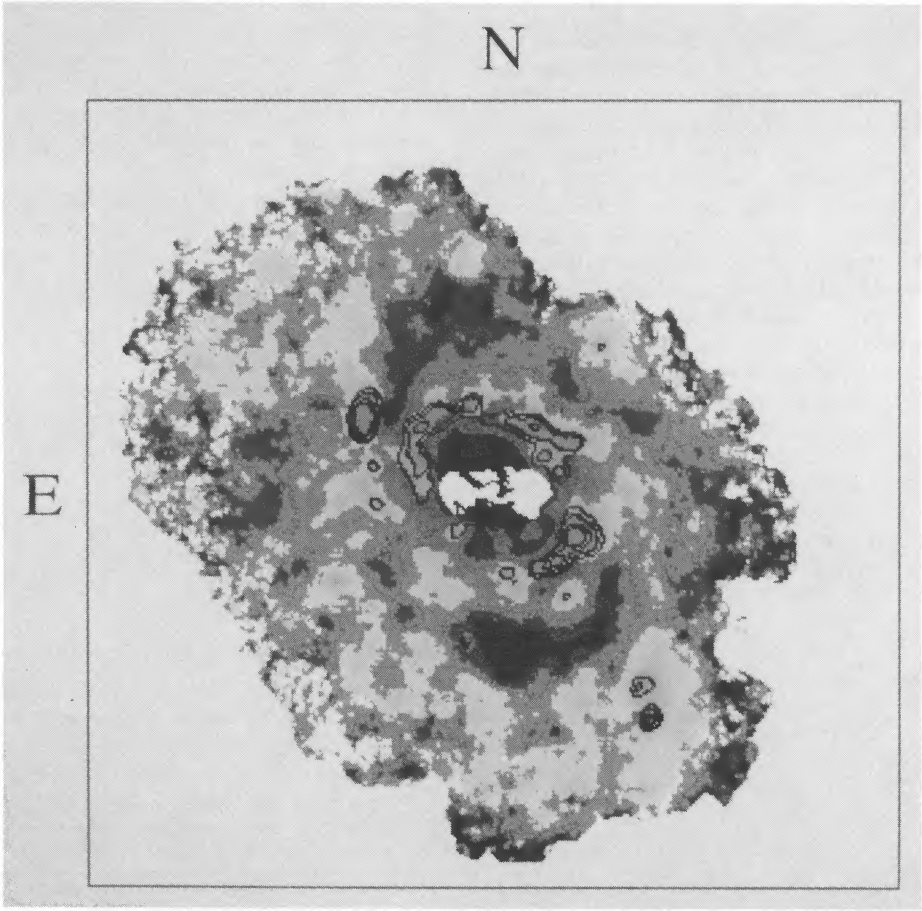

FIG. 1.—A composite image that shows both the distribution of the [N II] λ6584/Hα ratio and the brightest H II regions. The four shades of gray correspond to four ranges of the line ratio (from light to dark): 0.3–0.8, 0.8–1.3, 1.3–1.8, >1.8. The contours show the positions of the brightest H II regions and are always associated with low [N II] λ6584/Hα ratios (0.3–0.8). The discrete H II regions are embedded in a diffuse ionized medium characterized by higher [N II] λ6584/Hα line ratios (0.6–1.3). The highest values of [N II] λ6584/Hα are located near the nucleus, along the radio axis (P.A. ~ 45°) and in two diametric crescents that lie northeast and southwest of the nucleus beyong the starburst ring.

galaxy, the derived intrinsic and direct properties are model-dependent, while the observed scattered properties are not. With this input spectrum, scattering optical depth $\tau_S = 0.1$ and torus open solid angle $\Delta\Omega/4\pi = \frac{1}{4}$, we find the following luminosities:

$$L_S = 2.1 \times 10^{42} \text{ ergs s}^{-1} ,$$
$$L_I = 6.6 \times 10^{43} \text{ ergs s}^{-1} ,$$
$$L_D = 6.0 \times 10^{43} \text{ ergs s}^{-1} .$$

The intrinsic ionizing luminosity, L_I, is roughly one-quarter of the nuclear infrared luminosity of $1.5 \times 10^{11}\ L_\odot$ (Telesco et al. 1984). The total intrinsic number of photons emitted between 13.6 eV and 5 keV is

$$Q_I = \frac{L_I}{L_S}\int_{13.6\text{ eV}}^{5\text{ keV}} \frac{L_0}{h\nu}\,d\nu = \frac{L_I}{L_S}\,3.66 \times 10^{52} \text{ s}^{-1}$$
$$= 1.1 \times 10^{54} \text{ s}^{-1} .$$

An upper limit of 5 keV is used in this integration to facilitate comparison of ionization parameters calculated later, with photoionization model results limited to 5 keV maximum photon energy. Of the emitted photons, only $(\Delta\Omega/4\pi)Q_I$ propagate along the direct cones. Thus the number of ionizing, non-scattered photons streaming along the direct cones, $Q_D = 2.6 \times 10^{53}$ s^{-1}, while the number scattered from the direct cones, $Q_S = 2.7 \times 10^{52}$ s^{-1}.

Strömgren radii provide a rough idea of the distances out to which the direct and scattered nuclear emission can ionize the DIM. Paper II indicates that the filling factor and electron density in the DIM satisfy $\phi n_e^2 \simeq 0.01$. The direct and scattered Strömgren radii, R_D and R_S, are then 15 kpc and 5 kpc, respectively. These exceed the radii out to which we detect the DIM (Paper II) and disagree in ratio to that observed. The calculated ratio is primarily sensitive to the adopted value of τ_S and can only be brought into agreement with our observations for $\tau_S \sim 0.7$, a value prohibited by the observed polarization of the broad optical emission lines (Antonucci & Miller 1985). These discrepancies may arise from the penetrating ability of power-law continua and the associated presence of a significant partially ionized zone, the assumption of a pure hydrogen medium, intervening dust absorption, the detailed angular dependence of the scattering process or insufficient covering fraction of the DIM–emitting clouds to warrant a Strömgren sphere calculation. We have calculated the Strömgren radii of dusty H II regions and find that for $\sim$0.3 mag kpc^{-1} of dust extinction, the calculated Strömgren radius perpendicular to the direct cones agrees with the observed extent of the DIM.

3.2. *Energetics*

The total luminosities of [N II] λ6584 and Hα observed in Paper II from this DIM are $L_{\text{H}\alpha} = 1.2 \times 10^{41}$ ergs s^{-1} and $L_{[\text{N II}]} = 3.0 \times 10^{41}$ ergs s^{-1}, with about half emitted inside and half outside the direct cones. With no dust extinction, the total energy available within the direct cones in the range 13.6 eV to 15 keV is

$$E_D = \frac{\Delta\Omega}{4\pi} L_D = 1.5 \times 10^{43} \text{ ergs s}^{-1} ,$$

while that available outside of the direct cones is

$$E_S = \left(1 - \frac{\Delta\Omega}{4\pi}\right) L_S = 1.6 \times 10^{42} \text{ ergs s}^{-1} .$$

To approximate possible energy loss due to dust extinction, we have incorporated various values of extinction in calculating E_D^{dust} and E_S^{dust}, the dust-extinguished energy available to the DIM from the direct and scattered continua. We find

$$E_D^{\text{dust}} = E_D e^{-R_D^{\text{obs}}/r_0} ,$$
$$E_S^{\text{dust}} = E_S e^{-R_S^{\text{obs}}/r_0} ,$$

where R_D^{obs} and R_S^{obs} are the observed radii to which the DIM emission is observed along and perpendicular to the jet axis, and the extinction scale length r_0, is related to the value of the extinction E in mag kpc^{-1} by

$$E = -2.5 \log_{10} (e^{-1 \text{ kpc}/r_0}) .$$

We set $R_D^{\text{obs}} = 5.3$ kpc and $R_S^{\text{obs}} = 3.8$ kpc. Table 2 compiles values for E_D^{dust}, and E_S^{dust} for various values of the extinction E and r_0.

Photoionization models (§ 4) show that for ionization parameters in the range, $10^{-4.5} \leq U \leq 10^{-4.1}$, which is shown later are most appropriate for the DIM away from the direct cones, the emission from [N II] λ6584 and Hα supplies approximately 10% of the total cooling. Therefore, we estimate that the total energy, emitted by the DIM outside of the direct cones, is $\sim 1.5 \times 10^{42}$ ergs s^{-1}. The excellent agreement between the energy supplied by the scattered nuclear continuum is probably fortuitous. For moderate dust extinction with $r_0 = 5.43$ kpc and $r_0 = 2.71$ kpc, the available scattered energies are low by factors of $\sim$2 and $\sim$4, respectively. A more exact analysis of the energy budget in the DIM away from the direct cones is complicated by the following factors:

1. The necessity of determining the total luminosity by extrapolating the observed [N II] λ6584 and Hα luminosities from model results;
2. The measured ultraviolet and X-ray nuclear luminosities are uncorrected for internal extinction;
3. Possible nuclear emission at energies $E \geq 15$ keV (extrapolation of the nuclear spectrum to 1 MeV more than doubles the available energy);
4. Possible extranuclear (> 100 pc) scattering supplying significant energy to the DIM;
5. Possible supplemental heating sources for the DIM.

With these uncertainties in mind, we believe that the current energy constraints allow for no more than $\sim$0.3 mag kpc^{-1} of dust extinction within this DIM. The energy supply to the DIM in the direct cones is more than an order of magnitude greater than that off the cones and so appears sufficient to energize this component, but because of its extreme model dependence, we refrain from any detailed calculation of this energy budget.

3.3. *Ionization Parameters*

The physical state of a photoionized gas depends on the local gas density and the shape and intensity of the ionizing

TABLE 2

DUST-EXTINGUISHED ENERGIES

E (mag kpc^{-1})	r_0 (kpc)	E_D^{dust} (ergs s^{-1})	E_S^{dust} (ergs s^{-1})
0	∞	1.5×10^{43}	1.6×10^{42}
0.1.....	10.9	9.2×10^{42}	1.1×10^{42}
0.2.....	5.43	5.7×10^{42}	7.9×10^{41}
0.3.....	3.62	3.5×10^{42}	5.6×10^{41}
0.4.....	2.71	2.1×10^{42}	3.9×10^{41}
0.5.....	2.17	1.3×10^{42}	2.8×10^{41}

spectrum. For a given spectral shape, at densities low enough that collisional deexcitation is negligible, the effects of gas density and source intensity can be combined in the dimensionless ionization parameter U, defined as

$$U(r) = \frac{n_\gamma(r) \text{ photons cm}^{-3}}{n_e(r) \text{ electrons cm}^{-3}} = \frac{Q(r)}{4\pi r^2 c} \frac{1}{n_e(r)},$$

where $Q(r)$ is the total number of ionizing photons crossing a sphere of radius r per second. Therefore, at sufficiently low densities, the output spectrum of an ionization-bounded photoionized gas is determined by the source spectral shape and the ionization parameter at the illuminated side of the gas. A reduction in U, caused by a decrease in the source intensity, an increase in the distance between source and filament, or an increase in the ambient density of the filament, will result in a lowering of the excitation conditions within the gas.

To estimate the radial dependence of $U(r)$, we determine $Q(r)$ for various models with and without dust extinction. For comparison with our photoionization models we calculate $Q(r)$ in the spectral range 13.6 eV–5 keV. Four basic models are considered:

Model 1.—No dust extinction and simple geometrical dilution (equivalent to low covering fraction throughout the DIM);

Model 2.—No dust extinction with geometrical dilution and local hydrogen absorption (equivalent to high covering fraction throughout the DIM);

Model 3.—Dust extinction convolved with geometrical dilution;

Model 4.—Dust extinction convolved with geometrical dilution and local hydrogen absorption.

The ionization parameters for these, $U_{1-4}(r)$, are

$$U_1(r) = \frac{Q_0}{4\pi r^2 c} \frac{1}{n_e(r)},$$

$$U_2(r) = \frac{Q_0 - (\mathscr{A} r^3/3)}{4\pi r^2 c} \frac{1}{n_e(r)},$$

$$U_3(r) = \frac{Q_0 e^{-r/r_0}}{4\pi r^2 c} \frac{1}{n_e(r)},$$

$$U_4(r) = \frac{-\mathscr{A} r_0(r^2 - 2rr_0 + 2r_0^2) + (Q_0 + 2\mathscr{A} r_0^3)e^{-r/r_0}}{4\pi r^2 c} \frac{1}{n_e(r)},$$

where Q_0 is the number of initial ionizing photons, assuming isotropic emission and $\mathscr{A} = 4\pi\phi n_e^2 \alpha_B$, with $\alpha_B = 2.6 \times 10^{-13}$ cm^3 s^{-1}, the case B hydrogen recombination coefficient. The ionization parameters in the first three cases are straight forward while $U_4(r)$ is derived from the solution to the differential equation,

$$\frac{dQ(r)}{dr} = -\frac{Q(r)}{r_0} - \mathscr{A} r^2.$$

The intent of these models is only that the calculated ionization parameters be indicative of the ionization state of the DIM. Because models 1 and 4 represent the extremes of photon propagation, they yield upper and lower limits to the ionization parameters respectively. Since the densities in the DIM are as yet undetermined, we plot $U_1(r) \times n_e(r)$ and $U_4(r) \times n_e(r)$ in Figure 2 and tabulate their values for various radii and dust extinctions in Table 3. Previous workers (Evans & Dopita 1986; Bergeron et al. 1989) have noted that if the high-

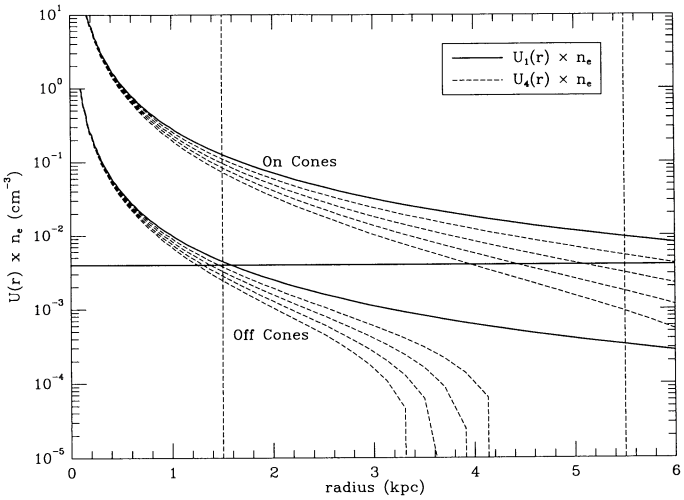

FIG. 2.—The product of a constant electron density (n_e) and the ionization parameter $U(r)$ as a function of radius inside and outside the region directly visible to the nucleus. The solid curves correspond to a change in $U(r)$ through geometric dilution alone [model $U_1(r)$]. The dashed curves correspond to the most extreme case of geometric dilution, local hydrogen absorption, and dust extinction [model $U_4(r)$] where the different curves are for (0.0, 0.1, 0.2, 0.3) mag kpc^{-1} of extinction. The vertical dotted lines delineate our radial region of interest between 1.5 and 5.5 kpc where the DIM is observed, while the horizontal solid line at $10^{-2.4}$ divides the figure into the two distinct regions within which the product $U(r) \times n_e$ on and off the direct cones resides. The boundary at $U(r) \times n_e = 10^{-2.4}$ separates the regions of high excitation along the direct cones from the low-excitation regions off the direct cones, demonstrating that the distinct excitation conditions on and off the cones must arise from a difference in the ionization parameter by a factor of ~ 30.

excitation gas in NGC 1068 is photoionized by a power-law continuum, then it may require a low energy spectral cutoff considerably higher than 13.6 eV to produce their observed [Ne v] ($\lambda\lambda$3346, 3426)/He II λ4686 line ratios. Evans & Dopita (ED87) find that power-law photoionization with a low energy cutoff of 540 eV best reproduces this line ratio. However, we believe the source of the anomalous [Ne v] ($\lambda\lambda$3346, 3426)/He II λ4686 ratio must lie elsewhere, as the measured nuclear continuum between 13.6 and 540 eV shows no hint of significant absorption, and such a cutoff, caused either by nuclear absorption (as favored in ED87), or by absorption within the DIM itself would be observed in the nuclear spectrum due to the distended nature of the DIM gas distribution (see § 3.5, below). Also such a cutoff would preclude photoionization as the source of observed gas excitation because this would drastically reduce the available energy supply to the DIM.

3.4. *Additional Emission Properties*

The spectroscopy of Evans & Dopita (ED87) further constrains the emission properties of this DIM. The 13 H II regions in their data reside outside the direct cones. They note that their spectra are composites of a bright H II region component and a less intense, diffuse ionized component. For such a composite spectrum, we can write the observed [N II] λ6584/Hα ratio as

$$\frac{I^{\text{obs}}_{[\text{N II}]}}{I^{\text{obs}}_{\text{H}\alpha}} = R^{\text{obs}} = \frac{I^{\text{diff}}_{[\text{N II}]} + I^{\text{H II}}_{[\text{N II}]}}{I^{\text{diff}}_{\text{H}\alpha} + I^{\text{H II}}_{\text{H}\alpha}},$$

where intensities are denoted by capital I; superscripts refer to emission as observed, from the H II region itself or from the diffuse component; and subscripts refer to the emitted line

TABLE 3

MODEL IONIZATION PARAMETERS

r	$U_1(r) \times n_e(r)$	$U_4(r) \times n_e(r)$		
		$r_0 = \infty$	$r_0 = 5.43$ (kpc)	$r_0 = 2.71$ (kpc)
Inside the Direct Cones				
500 pc	1.2	1.2	1.0	9.5×10^{-1}
1 kpc	2.9×10^{-1}	2.9×10^{-1}	2.4×10^{-1}	2.0×10^{-1}
2 kpc	7.2×10^{-2}	7.2×10^{-2}	5.0×10^{-2}	3.4×10^{-2}
3 kpc	3.2×10^{-2}	3.2×10^{-2}	1.8×10^{-3}	1.0×10^{-3}
4 kpc	1.8×10^{-2}	1.8×10^{-2}	8.4×10^{-3}	4.0×10^{-3}
5 kpc	1.2×10^{-2}	1.1×10^{-2}	4.4×10^{-3}	1.6×10^{-3}
6 kpc	8.0×10^{-3}	7.7×10^{-3}	2.4×10^{-3}	6.9×10^{-4}
Outside the Direct Cones				
500 pc	4.1×10^{-2}	4.1×10^{-2}	3.7×10^{-2}	3.4×10^{-2}
1 kpc	1.0×10^{-2}	1.0×10^{-2}	8.5×10^{-3}	7.0×10^{-3}
2 kpc	2.6×10^{-3}	2.5×10^{-3}	1.7×10^{-3}	1.1×10^{-3}
3 kpc	1.1×10^{-3}	1.0×10^{-3}	5.2×10^{-4}	2.6×10^{-4}
4 kpc	6.4×10^{-4}	4.4×10^{-4}	1.4×10^{-4}	5.0×10^{-6}

type. Defining

$$\eta = I^{\rm diff}_{\rm H\alpha}/I^{\rm H\,II}_{\rm H\alpha} ,$$

$$R^{\rm H\,II} = I^{\rm H\,II}_{\rm [N\,II]}/I^{\rm H\,II}_{\rm H\alpha} ,$$

$$R^{\rm diff} = I^{\rm diff}_{\rm [N\,II]}/I^{\rm diff}_{\rm H\alpha} .$$

The observed [N II] λ6584/Hα ratio can be written as

$$R^{\rm obs} = \frac{(\eta \times R^{\rm diff}) + R^{\rm H\,II}}{\eta + 1} .$$

The solution for η is

$$\eta = \frac{R^{\rm obs} - R^{\rm H\,II}}{R^{\rm diff} - R^{\rm obs}} .$$

Values for $R^{\rm obs}$ come from ED87, values for $R^{\rm diff}$ are measured from around the individual H II regions in the [N II] λ6584/Hα ratio map of Figure 1, and because the H II region abundances are known to be solar (ED87), we assume that each H II region emits a "canonical" value of [N II] λ6584/Hα = 0.3. For any other forbidden line which exists in the data in ED87, we can write the intrinsic emission ratio with respect to Hα from the high-excitation component as

$$R^{\rm diff}_{\rm forb} = \frac{R^{\rm obs} \times (\eta + 1) - R^{\rm H\,II}_{\rm forb}}{\eta} ,$$

where $R^{\rm H\,II}_{\rm forb}$ is the assumed line ratio for the H II region. Evans & Dopita (ED87) supply complete data for the lines [O II] λ3727, [O III] $\lambda\lambda$4959, 5007, and [S II] $\lambda\lambda$6716, 6731 so by assuming H II region emission ratios for these lines of 0.7, 0.8, and 0.08 respectively (Evans & Dopita 1985), we can determine the intrinsic emission properties of the DIM for each of these lines. Because of the complexities of this analysis, we have averaged the line emission characteristics in these lines from the DIM over the 13 H II regions. We find that the DIM outside the direct cones is characterized by the following line ratios:

$$\text{[N II] } \lambda6584/\text{H}\alpha = 1.1 \pm 0.2 ,$$

$$\text{[O II] } \lambda3727/\text{H}\alpha = 1.0 \pm 0.5 ,$$

$$\text{[O III]}(\lambda4959 + \lambda5007)/\text{H}\alpha = 0.4 \pm 0.2 ,$$

and

$$\text{[S II]}(\lambda6716 + \lambda6731)/\text{H}\alpha = 0.4 \pm 0.1 .$$

3.5. *Geometry and Implications*

The geometry of the nuclear region in NGC 1068 is ultimately responsible for many of the observed properties of the DIM in this galaxy. Our adopted geometry is that determined in Paper I where the emission from the nuclear regions is optimally modeled by bipolar conical outflows of opening angle $\simeq 80°$, with projected symmetry axis position angle $\simeq 45°$. The symmetry axis is found to be inclined to the plane of the galaxy by $\simeq 45°$, with the NE cone being out of the plane of the sky and the SW cone into the plane. If we assume that the outflow geometry is derived from the underlying torus geometry, then this has several important consequences. The polarization this implies is $\geq 50\%$, significantly greater than that measured in NGC 1068 by Antonucci & Miller (1985), and in several other Seyfert 2 galaxies (Miller & Goodrich 1990). Improper background subtraction in the spectropolarimetry work may account for this discrepancy or it may be that tori are leaky, allowing some light to penetrate through, thereby reducing the polarization. This would not affect our model results except to reduce the direct and intrinsic luminosities by a factor of ≤ 3. As these values are highly model-dependent, and because there seems to be ample flux in the direct cones to energize that portion of the DIM, this is of little consequence. However, the presence of a leaky torus is not supported by the ratio of X-ray continuum luminosities to polarized broad line luminosities (Lawrence 1987).

Another implication of our adopted nuclear geometry is that the nuclear emission is not restricted to the plane of the galaxy. This requires that the DIM gas distribution be significantly thicker than the galaxy disk in order to intercept all of the available energy from the photon field. There is evidence that this gas distribution is indeed highly distended. For a photoionized DIM, the presence of high [N II] λ6584/Hα ratios beyond the starburst ring implies a distribution of the DIM gas significantly greater than that of the ring itself to avoid significant attenuation. Bergeron et al. (1989) find that the kinematics of the high-excitation gas along the jet axis deviates from the underlying disk rotation. Their interpretation is that the high-

excitation gas has a thickness of ~ 1 kpc. Also the line widths of the diffuse gas in our Fabry-Perot data (150–250 km s^{-1} FWHM) are suggestive of a puffed-up distribution ($z_0 \geq 400$ pc; Paper II) of DIM material when compared with neighboring H II region line widths (50–150 km s^{-1}; Paper II). Understanding the source of this high–scale-height ($|z|$) gas in NGC 1068 is important for generalizing our understanding to other active galaxies.

NGC 1068 contains an annulus of starburst activity presumably confined by the action of the stellar bar. This annulus has a radius of ~ 1.5 kpc, and an IR luminosity of 1.5×10^{44} ergs s^{-1}, a factor of 10 times that of another powerful starburst system M82 (Telesco & Harper 1980). By analogy with M82 (Bland & Tully 1988), supernovae associated with the starburst ring could produce a prodigious outflow of ejecta, blowing away from the annulus and extending out to high galactic latitudes. If this gas is gravitationally bound, it can cool and rain back onto the disk, forming a thick layer of diffuse gas. Whether this ejecta is gravitationally bound or not is unknown, but it is a potential source of large quantities of matter for the DIM in NGC 1068. For galaxies with less active star formation, ejecta from both individual and associations of supernovae may be able to generate smaller fountains, thereby accumulating significant gas at large scale heights via the sum of many such single, isolated outflows (Corbelli & Salpeter 1988). Also, near-nuclear gas heated directly by the nuclear continuum and driven outward by thermal expansion and/or radiation pressure is another potential source of DIM gas (Begelman 1985). Evidence for gas at high $|z|$ in our Galaxy as well as other galaxies is beginning to mount (Cox & Reynolds 1987; Reynolds 1988, 1990; Dettmar 1990), suggesting that diffuse, high–$|z|$ gas may be commonplace.

3.6. *Scattering Mechanism*

Fabry-Perot observations (Paper II) indicate for the first time the presence of significant ionized gas not associated with H II regions away from the radio axis in NGC 1068. We have examined both electron- and dust-scattering mechanisms for their ability to scatter ionizing radiation out of the direct cones into the extended disk. In Figure 3*a*, the relative efficiency of stationary electrons in scattering photons has been computed as a function of photon energy and scattering angle from the Klein-Nishina cross section. In Figure 3*b*, an analogous plot is shown for scattering by dust particles. Since the grain composition of any external galaxy is unknown, we have used the MRN model composition which successfully explains the "standard" extinction curve in terms of the absorption and scattering properties of graphite and silicate grains. We adopt a power-law distribution of grain sizes (Draine & Lee 1984) that lie within the range $0.005 \leq a \leq 1$ μm (MRN) for which

$$dn = (A_{Si} + A_C) n_H a^{-3.5} da$$

and where $n_H = 5.8 \times 10^{21} E_{B-V}$. The carbon and silicate abundances are those used in MRN which are $\log A_C = -25.13$ and $\log A_{Si} = -25.10$. The angular dependence of the dust scattering has been derived from the Henyey-Greenstein phase function (Hansen 1969; Martin 1978). The dielectric grain properties as a function of energy, kindly supplied by B. T. Draine (0–40 eV) and P. G. Martin (10^{-3} to 10^4 eV), reveal that the MRN mixture is almost entirely forward-scattering beyond the Lyman limit (Martin & Rouleau 1990). This has the important consequence that dust is unable to scatter significant ionizing radiation into the extended disk. Figure 3*b* shows both the dramatic energy and angular dependence of dust scattering. The progressively forward nature of dust scattering with increasing energy produces values of U off the direct cones one or two orders of magnitude below those required for the production of [N II] λ6584/Hα ratios appreciably above 0.1, and also introduces strong wavelength dependence not seen in the nuclear continuum out to 15 keV. The disk of NGC 1068 is known to be very dusty (Smith, Weedman, & Spinrad 1972), and Miller (1989) reports the

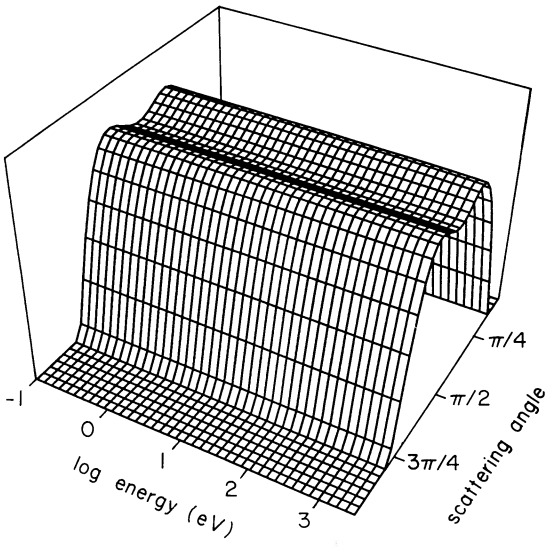

FIG. 3*a*

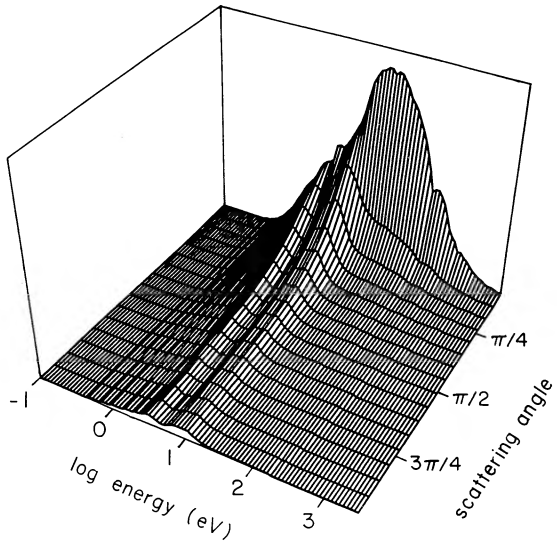

FIG. 3*b*

FIG. 3.—A comparison of the efficiency of stationary electrons and dust grains in scattering photons plotted as a function of the logarithm of the photon energy (eV) and scattering angle (radians): (*a*) electron scattering derived from the Klein-Nishina cross section; (*b*) scattering by the Mathis, Rumpl, & Nordsieck (1977) composition of graphite and silicate grains where the angular dependence is derived from the Henyey-Greenstein phase function. Pure forward scattering occurs at an angle of 0°, while backward scattering occurs at 180° although these extremes are not shown in (*b*). The dust scattering efficiencies are shown in 10° increments between 10° and 170°.

detection of a dust-scattering cloud located 5″ from the nucleus, so that some extranuclear dust scattering is to be expected on 100 pc to kiloparsec scales. This can lead to some hardening of the continuum along the direct cones although not enough to depopulate totally the low-energy end of the photon spectrum and produce the observed [Ne v] λλ3346, 3426 and He II λ4688 intensities. This does not change our model results for the excitation of the DIM away from the direct cones as the scattered spectrum is fixed by observation. However, a harder spectrum along the direct cones could have observable consequences which are discussed in § 4.

Figure 3*a* shows that Thomson scattering is essentially independent of wavelength and scatters preferentially into angles between 40° and 140°. This allows for the extended disk ISM away from the radio axis to be evenly illuminated by the electron-scattered nuclear continuum reproducing the observed lack of azimuthal variation in the [N II] λ6584/Hα ratio. These data therefore strongly favor Thomson scattering as the mechanism responsible for scattering ionizing radiation into the DIM away from the direct cones. Other observations buttress this conclusion. The measured X-ray continuum seen out to 15 keV with a near-canonical AGN power-law index of ~ -0.5, the X-ray continuum luminosity to polarized broad-line luminosity ratio typical of a Seyfert 1 (Lawrence 1987), and the detection of the Fe Kα line at 6.5 keV (Koyama et al. 1989) all support the existence of a large population of free electrons within the circumnuclear regions.

4. PHOTOIONIZATION MODELING

4.1. *Model Parameters*

Due to its large spatial extent and inevitable variations in local gas properties, we choose not to model in detail the distribution of emission from the DIM in NGC 1068. Instead we explore the parameter space available to individual filaments of a DIM using sets of photoionization models computed with the ionization code MAPPINGS (Binette 1982; Binette, Dopita, & Tuohy 1985). The model photoionizing continua are one-component power laws with spectral indices, $\alpha = -0.5$, -1.0, -1.5 and -2.0, with continuum photon energies from 7.6 eV to 5 keV. Such high-energy photon components are necessary to produce the observed, elevated [N II] λ6584/Hα ratios, because models with continua terminated at 29.5 eV (below the ionization potential of N^+) result in [N II] λ6584/Hα distributions which rise monotonically with U only to reach asymptotic limits of ≤ 0.5. Physically this is the result of the fact that limited electron temperatures are produced with lower energy photons, thereby limiting the number of metastable-state collisional excitations per electron-proton recombination. The elevated temperatures, obtainable with higher energy photons, are therefore necessary to yield very high (≥ 0.5) [N II] λ6584/Hα ratios. Furthermore, it is the higher energy photons which, due to their lower cross sections, penetrate deeper into the slab producing a partially ionized zone (Ferland & Netzer 1983; Halpern & Steiner 1983; Binette 1985) where charge exchange and secondary electron heating boost the emission from lower ionization species (e.g., S^+, N^+, O^+).

Stauffer (1982) and Rose & Searle (1982) find that filling factors in LINERs and extended emission-line regions in external galaxies are $10^{-4} \leq \phi \leq 10^{-6}$. This implies that the separation between nuclear source and emitting element will be much greater than the physical extent of the element itself. These models therefore use plane-parallel geometry throughout. These filling factors also imply particle densities of 10–100 cm^{-3} in the DIM of NGC 1068, well below the critical densities for all major ionic species. The models therefore explore the low-density regime, using isobaric density profiles and hydrogen densities of 1 cm^{-3} at the illuminated face of the slab and filling factors of unity. All of the models are ionization-bounded, being terminated when the H^+/H^0 ratio falls below 0.01. The radiation field is specified by the ionization parameter U at the front face of the slab, and the spectral index α, where the monochromatic intensity varies with photon energy as E_γ^α. These models span the range $10^{-6} \leq U \leq 10$.

4.2. *Model Results*

Model results are shown in Figures 4*a*–4*f*. To facilitate comparison with the measured [N II] λ6584/Hα and other inferred line ratios, we plot line intensities relative to Hα versus ionization parameter U throughout, despite the strong temperature variations these contain. In effect, much of the structure in these plots is produced by the varying temperature structure throughout the slabs modeled, so this will be noted where appropriate.

Figure 4*a* shows that the peak [N II] λ6584/Hα ratio is found within $2 \times 10^{-4} \leq U \leq 7 \times 10^{-4}$ for our range of α. The rise in [N II] λ6584/Hα with increasing U from $U \simeq 10^{-6}$ to $U \simeq 10^{-4}$ is similar for all four spectral indices, but the drop in [N II] λ6584/Hα with a further increase in U becomes more gradual for flatter continua. This widens the [N II] λ6584/Hα distribution with increasing (less negative) spectral indices. Examination of the ionization structure of the models shows that the rise in the [N II] λ6584/Hα ratio with U for $10^{-6} \leq U \leq 7 \times 10^{-4}$ is due primarily to an increase in the electron temperature throughout the slab with U. In this regime the shape of the N^+ zone correlates closely with the H^+ zone. This is due to the similarity in the ionization potentials of H^0 and N^0 and to the absence of a significant N^{++} zone at these low values of U. The average temperature in the N^+ zone continues to increase with U beyond $U \simeq 7 \times 10^{-4}$, but the [N II] λ6584/Hα ratio begins to fall here because a sufficiently large N^{++} zone now exists in the front of the slab. As there is no higher ionization state than H^+, the integrated emision of [N II] λ6584 falls with respect to Hα. The observed increase in the peak value of [N II] λ6584/Hα with increasing α is due to the increasing average temperatures of the spatially coincident N^+ and H^+ zones for $U \leq 7 \times 10^{-4}$. The shoulder visible on the $\alpha = -0.5$ plot at $7 \times 10^{-2} \leq U \leq 7 \times 10^{-1}$ is due to the extended, partially ionized N^0/N^+ zone deep inside the slab associated with the increasing predominance of higher energy photon absorption and subsequent secondary electron heating for flatter spectra.

Figure 4*b* shows the distribution of [S II] (λ6716 + λ6731)/Hα with U. It is apparent that, for a given α, the [S II] (λ6716 + λ6731)/Hα ratio is less sensitive to changes in U than [N II] λ6584/Hα over the range $10^{-5} \leq U \leq 10^{-2}$. This is due to the fact that for power-law photoionization, the primary [S II] λλ6716, 6731–emitting zones are thicker and located deeper within the slabs, primarily in the partially ionized zone, than are the corresponding [N II] λ6584– and [O II] λ3727–emitting zones. Due to the penetrating power of high-energy photons in a power-law spectrum, the S^+ zone can occupy as much as 90% of the depth of the slab. This results in the ability of power-law models to generate [S II] (λλ6716, 6731)/Hα ratios far in excess of those seen in H II regions.

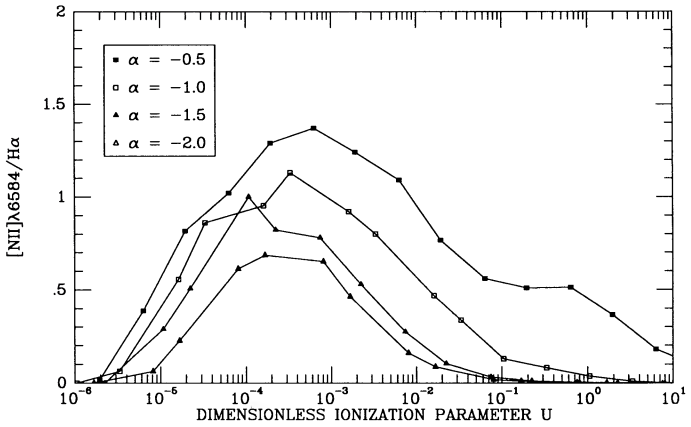

FIG. 4*a*

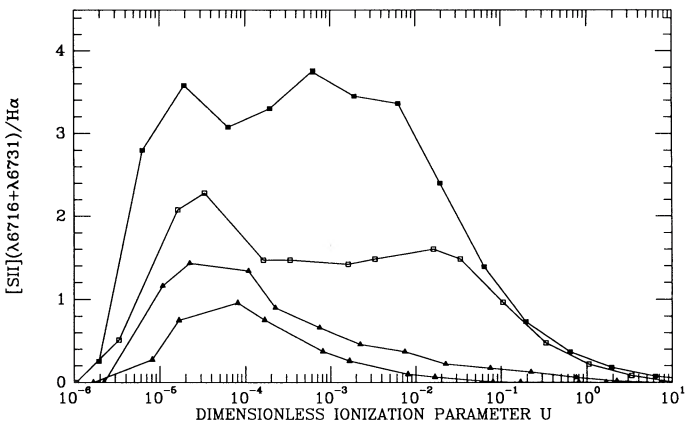

FIG. 4*b*

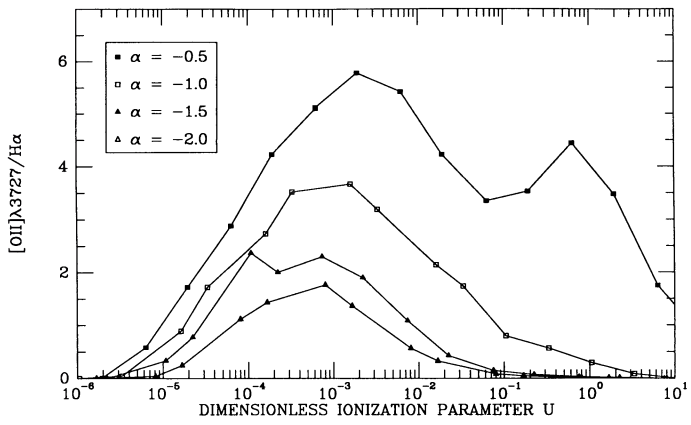

FIG. 4*c*

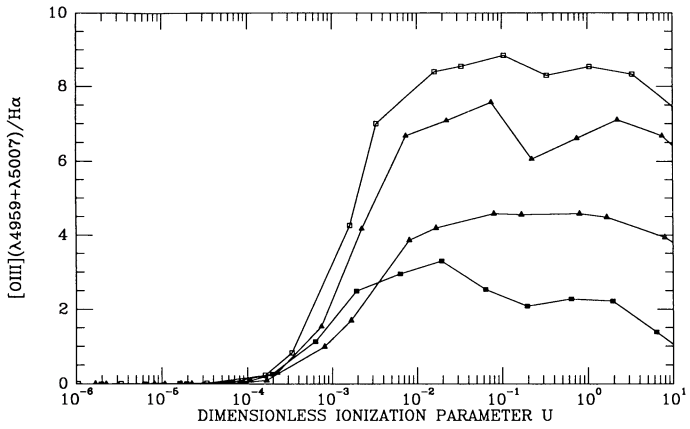

FIG. 4*d*

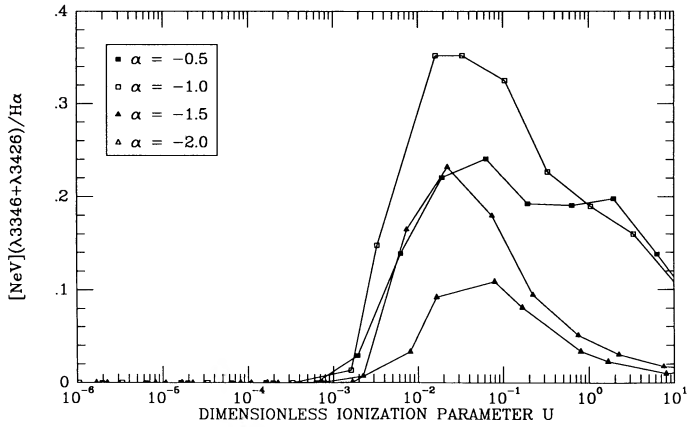

FIG. 4*e*

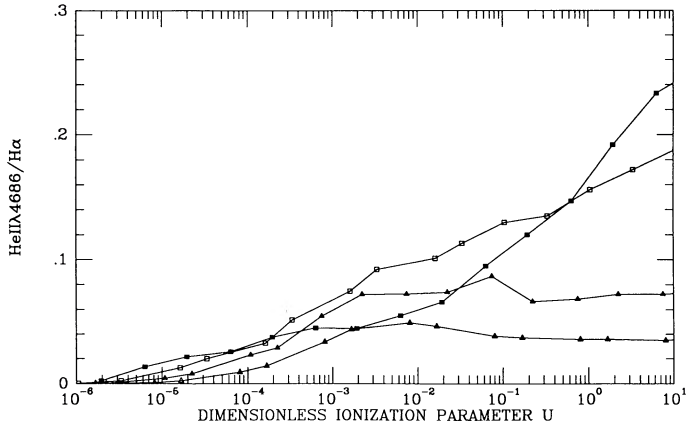

FIG. 4*f*

FIG. 4.—The computed strength of forbidden lines in ratio with Hα arising from power-law photoionization for a wide range in ionization parameter (10^{-6} to 10). For each line ratio, four values of the spectral index ($\alpha = -0.5, -1.0, -1.5, -2.0$) are used. The computed line ratios are (*a*) [N II] λ6584/Hα; (*b*) [S II] (λ6716 + λ6731)/Hα; (*c*) [O II] λ3727/Hα; (*d*) [O III] (λ4959 + λ5007)/Hα; (*e*) [Ne V] (λλ3346, 3426)/Hα; (*f*) He II λ4686/Hα. The plots facilitate a direct comparison between the observed line strengths from NGC 1068 and those expected from gas photoionized by a power-law ionizing source.

Figures 4*c* and 4*d* present the [O II] λ3727/Hα and [O III] (λ4959 + λ5007)/Hα ratio distributions with U. Figure 4*c* is qualitatively similar to Figure 4*a* but shifted slightly toward higher ionization parameters. This reflects the higher ionization potential of O^+ with respect to N^+, which is larger than the difference in the O^0 and N^0 ionization potentials, as well as the increased predominance of charge exchange reactions suppressing the O^+/O^0 ratio at low ionization fraction. It can be seen from Figures 4*c* and 4*d* that the [O III] (λ4959 + λ5007)/Hα ratio increases significantly where the [O II] λ3727/Hα ratio begins to fall. This reflects the shift in ionization structure away from O^+ to O^{++} in the front of the slab for higher

ionization parameters. The marked decrease in the [O III] ($\lambda 4959 + \lambda 5007$)/H$\alpha$ ratio for models with $\alpha = -0.5$ over those with steeper spectra, is currently being investigated.

Figure 4*e* shows the [Ne V] ($\lambda\lambda 3346$, 3426)/Hα ratio plotted against U. For all four spectral indices, the [Ne V] ($\lambda\lambda 3346$, 3426)/Hα ratio rises rapidly at $U \sim 10^{-3}$, then starts to fall at $U \sim 2 \times 10^{-2}$. This behavior is qualitatively different from the [O III] ($\lambda 4959 + \lambda 5007$)/H$\alpha$ plot of Figure 3*d* which holds approximately steady for $U \geq 10^{-2}$. Figure 4*e* also shows a decline in the peak value of [Ne V] ($\lambda\lambda 3346$, 3426)/Hα ratio for $\alpha = -0.5$. The He II $\lambda 4686$/Hα ratio is plotted in Figure 4*f*. We see a monotonic rise in this ratio with ionization parameter indicative of the increased ionization conditions with U. The slope of the plot increases for increasing α except for $\alpha = -0.5$, in the range $10^{-4} \leq U \leq 10^{-2}$, where at $U = 10^{-2}$ the slope again increases.

4.3. *Comparison with the DIM of NGC 1068*

The observed r^{-2} decrease of [N II] $\lambda 6584$ and Hα surface brightnesses (Paper II) suggests that for approximately constant ionization conditions there is a $\sim r^{-1}$ fall off in gas density. When convolved with the r^{-2} geometrical dilution of the radiation field, this produces a radial fall in the ionization parameter as $\sim r^{-1}$. The [N II] $\lambda 6584$/Hα ratio map of Figure 1 indicates that for radii greater than 1.5 kpc, the [N II] $\lambda 6584$/Hα ratio shows little systematic azimuthal variation. Figure 2 and Table 3 indicate that there is a factor of ~ 30 difference in the ionization parameter on and off the cones for a given radius, so then to reduce azimuthal variations in [N II] $\lambda 6584$/Hα, the ionization parameters on and off of the direct cones should straddle the peak in the [N II] $\lambda 6584$/Hα ratio plot. We find it optimal to set the electron density, $n_e \simeq 30$ cm^{-3} at 2 kpc, with an r^{-1} radial fall off. For these densities the values found in Table 3 indicate that the ionization parameters off the direct cones should vary between $10^{-4.5} \leq U \leq 10^{-4.1}$, for distances from 2 to 4 kpc, and the ionization parameters in the direct cones should fall in $10^{-3.1} \leq U \leq 10^{-2.6}$, for distances from 2 to 6 kpc. For this range of densities, the necessary filling factors are $10^{-5} \leq \phi \leq 10^{-4}$, and the model slab thicknesses, t, are $0.1 \leq t \leq 100$ pc.

Table 4 summarizes the comparison between the observed properties of the DIM and the model results. Comparing the model results with measured and derived ratios, it can be seen that for spectral indices $\alpha = -2.0$ to -1.5, those most representative of the low-energy/high-interaction end of the nuclear spectrum in NGC 1068, and for densities of $10 \leq n_e \leq 30$ cm^{-3}, these models produce $0.5 \leq$ [O II] $\lambda 3727$/H$\alpha \leq 2.5$ and [O III] ($\lambda 4959 + \lambda 5007$)/H$\alpha \leq 0.2$, in agreement with those observed. Ratios of $0.8 \leq$ [S II] ($\lambda 6716 + \lambda 6731$)/H$\alpha \leq 1.4$ are produced by the models which are slightly in excess of those observed. These [S II] ($\lambda 6716 + \lambda 6731$)/H$\alpha$ results can be interpreted as evidence that the emitting filaments in the DIM are actually smaller than our ionization-bounded models, which would tend to cut out a portion of the partially ionized zone where the majority of [S II] $\lambda\lambda 6716$, 6731 is produced. Observed values of [O II], [O III], and [S II] to Hα ratios along the direct zones are taken from Bergeron et al. (1988), where data for three individual regions are listed. The authors note that these values seem to have H II region emission superposed upon them so may not be truly representative of pure DIM emission.

TABLE 4

COMPARISON OF OBSERVED AND MODEL PROPERTIES

	Off Cones		On Cones	
Line Ratio	Observed	Model	Observed	Model
[N II]/Hα	0.6–1.3	0.4–1.0	0.6–2.5	0.4–0.8
[S II]/Hα	0.4 ± 0.1	0.8–1.4	0.3–0.4	0.3–0.7
[O II]/Hα	1.1 ± 0.6	0.5–2	0.8–1.0	1–2.5
[O III]/Hα	0.4 ± 0.2	≤ 0.1	1.2–2.8	1–5

Similar analysis of model [N II] $\lambda 6584$/Hα ratios would indicate that values of $0.4 \leq$ [N II] $\lambda 6584$/H$\alpha \leq 1.0$ are generated for the range of U appropriate for this DIM. These agree well with those observed over most of the disk, with only a slight shortfall at the high end where values of up to 1.3 are observed. Because the nuclear spectrum of NGC 1068 flattens above $\simeq 1$ keV to a power law of spectral index $\simeq -0.5$, the results of Figure 1*a* suggest that the multicomponent nuclear spectrum of NGC 1068 is itself able to produce the [N II] $\lambda 6584$/Hα ratios observed throughout the general disk. Also, the metal abundances in NGC 1068 may be enhanced by up to 30% to account for this discrepancy. It may also be that there are supplemental, global heating mechanisms operating which help produce the observed ratios. Mechanical and turbulent heating associated with supernovae in the starburst ring, and the *in situ* stellar population are possible sources of global heating. Leakage of ionizing photons from disk H II regions, and the high-energy (above 5 keV) nuclear luminosity would also supply additional heat to the DIM. However, our model [N II] $\lambda 6584$/Hα results are well below the highest ratios of up to 2.5 seen near the nucleus and in the crescents just beyond the starburst ring, indicating that there may be supplemental heating mechanisms operating anisotropically within the DIM of NGC 1068. Such possible anisotropic heating sources include mechanical heating associated with mass outflow from the nucleus (Paper I) as well as heating from the relativistic electron population responsible for the observed jet synchrotron emission (Ferland & Mushotzky 1984).

5. SUMMARY

Recent spectropolarimetry has demonstrated the existence of "buried" type 1 Seyfert nuclei, obscured from direct view, in NGC 1068 and a number of other type 2 Seyfert galaxies. The obscuring medium is most simply modeled as a torus, located between the broad-line region and the narrow-line region, that allows light to propagate only along bipolar openings (direct cones). In this picture, the broad-line region seen in polarized light and the visible–to–X-ray nuclear continuum have been redirected into our line of sight by optically thin, near-nuclear (≤ 100 pc) scattering regions located above the polar openings of the torus. The implied nuclear structure in NGC 1068, with opening angle $\simeq 80°$ and scattering optical depth $\tau_S \simeq 0.1$, produces an anisotropic, two-component radiation field, the intensity within the direct cones being more than an order of magnitude greater than outside the direct cones.

In recent years, long-slit observations of NGC 1068 have revealed high-excitation gas characterized by strong [O III], [Ne V], and He II emission confined to $\sim 40°$ from the radio jet axis and thought to be photoionized by nuclear continuum. In Paper II, we showed from imaging Fabry-Perot spectrophotometry that a vertically distended, diffuse ionized medium (DIM), with [N II]/Hα emission ratios much higher than in adjacent disk H II regions, exists throughout the inner ~ 10 kpc

disk of NGC 1068. In the present paper, we have examined a model of excitation of the roughly solar abundance DIM by the direct and scattered nuclear continua and find this a natural explanation for many of the observed emission characteristics. In particular, this model reproduces the magnitudes (0.6–1.3) and distribution of the [N II] λ6584/Hα ratios mapped across much of the DIM as well as the strength of other low-excitation species. Interestingly, while the models explain the strength of high-ionization lines close to the radio axis, the highest [N II] λ6584/Hα ratios (1.3–2.5) that are found almost exclusively in the same direction would seem to require an additional source of excitation.

Future optical Fabry-Perot studies will provide excellent tests of the accuracy of the obscuring torus model in NGC 1068. In particular, recent Fabry-Perot observations of the [O III] λλ4959, 5007 and Hβ spectral region should provide a superior excitation discriminant because the ionization parameters throughout the disk, while yielding azimuthally invariant [N II] λ6584/Hα ratios, produce [O III] (λλ4959, 5007)/Hβ ratios with an order of magnitude variation on and off the direct cones. These data will constrain further the excitation conditions throughout the DIM in addition to shedding light on the nuclear geometry and supplemental heating mechanisms operating along the radio axis.

We believe that Fabry-Perot observations of NGC 1068 demonstrate that an active galactic nucleus can have a significant influence on the large-scale ISM of a host galaxy. Recent theoretical developments suggest that electron scattering regions are a natural consequence of ablation by active nuclei on their environments (Krolik & Begelman 1986). In this event, regardless of the orientation of the obscuring torus to the disk plane, we conjecture that large-scale heating by the nucleus of the disk ISM in active galaxies may be common.

J. K. S. and J. B. H. are partially funded through NSF grant AST 88-18900 that supports the HIFI "Nearby Active Galaxies" program. We are grateful to Mike Dopita and Gary Ferland for access to the ionization codes MAPPINGS and CLOUDY, and to Rick Pogge and Gary Hill for VMS machine time for much of our modelling. We have benefited greatly from conversations with Rice colleagues Jon Weisheit and Reggie Dufour and with Ski Antonucci, Luc Binette, Mike Dopita, Ian Evans, Gary Ferland, Bob Goodrich, and Andrew Wilson. We acknowledge and deeply appreciate the contributions of Peter Martin and Bruce Draine for supplying the dielectric functions of dust gains on short notice. This work was undertaken to fulfill part of the research requirements for the Ph.D. degree at Rice University.

REFERENCES

Antonucci, R. R. J., & Miller, J. S. 1985, ApJ, 297, 621
Bailey, J., Axon, D. J., Hough, J. H., Ward, M. J., McLean, I., & Heathcote, S. R. 1988, MNRAS, 234, 899
Baldwin, J. A., Wilson, A. S., & Whittle, M. 1987, ApJ, 319, 84
Baum, S. A., & Heckman, T. 1989, ApJ, 336, 681
Begelman, M. C. 1985, ApJ, 297, 492
Bergeron, J., Petitjean, P., & Durret, F. 1989, A&A, 213, 61
Binette, L. 1982, Ph.D. thesis, Australian National University
———. 1985, A&A, 143, 334
Binette, L., Dopita, M. A., & Tuohy, I. R. 1985, ApJ, 297, 476
Bland, J., & Tully, R. B. 1988, Nature, 334, 43
Bland-Hawthorn, J., et al. 1991, in preparation
Bland-Hawthorn, J., Sokolowski, J., & Cecil, G. 1991, ApJ, 375, 78 (Paper II)
Bohlin, R. C., & Savage, B. D. 1981, ApJ, 249, 109
Cecil, G., Bland, J., & Tully, R. B. 1990, ApJ, 355, 70 (Paper I)
Corbelli, E., & Salpeter, E. E. 1988, ApJ, 326, 551
Cox, D. P., & Reynolds, R. J. 1987, ARA&A, 25, 303
de Grijp, M. H. K., Miley, G. K., Lub, J., & de Jong, T. 1985, Nature, 314, 240
Dettmar, R. J. 1990, A&A, 232, L15
Draine, B. T., & Lee, H. M. 1984, ApJ, 285, 89
Elvis, M., & Lawrence, A. 1988, ApJ, 331, 161
Evans, I. N., & Dopita, M. A. 1985, ApJS, 58, 125
———. 1986, ApJ, 310, L15
———. 1987, ApJ, 319, 662 (ED87)
Ferland, G. J., & Mushotzsky, R. F. 1984, ApJ, 286, 42
Ferland, G. J., & Netzer, H. 1983, ApJ, 264, 105
Halpern, J. P., & Steiner, J. E. 1983, ApJ, 269, L37
Hansen, J. E. 1969, J. Atmos. Sci., 26, 478
Koyama, K., Inoue, H., Tanaka, Y., Awaki, H., Takano, S., Ohashi, T., & Matsuoka, M. 1989, PASJ, 41, 731
Krolik, J. H., & Begelman, M. C. 1986, ApJ, 308, L55
Lawrence, A. 1987, PASP, 99, 309
Martin, P. G. 1978, Cosmic Dust (Oxford: Oxford University Press)
Martin, P. G., & Rouleau, F. 1990, preprint
Mathis, J. S., Rumpl, W., & Nordsieck, K. H. 1977, ApJ, 217, 425 (MRN)
Myers, S. T., & Scoville, N. Z. 1987, ApJ, 312, L39
Miller, J. S. 1989, in IAU Symposium 134, Active Galactic Nuclei, ed. D. E. Osterbrock & J. S. Miller (Dordrecht: Kluwer), p. 273
Miller, J. S., & Goodrich, R. W. 1990, ApJ, 355, 456
Monier, R., & Halpern, J. P. 1987, ApJ, 315, L17
Nishimura, M., Kaneko, N., & Toyama, K. 1984, A&A, 130, 46
Osterbrock, D. E., & DeRobertis, M. M. 1985, PASP, 97, 902
Pogge, R. 1988, ApJ, 328, 519
Reynolds, R. J. 1988, ApJ, 333, 341
———. 1990, ApJ, 349, L17
Robinson, A., Binette, L., Fosbury, R. A. E., & Tadhunter, C. N. 1987, MNRAS, 227, 97
Rose, J. A., & Searle, L. 1982, ApJ, 253, 556
Scoville, N. Z., Young, J. S., & Lucy, L. B. 1983, ApJ, 270, 443
Smith, M. G., Weedman, D. W., & Spinrad, H. 1972, Ap Letters, 11, 21
Spinrad, H., & Djorgovski, S. 1984, ApJ, 285, L49
Stauffer, J. R. 1982, ApJ, 262, 66
Telesco, C. M., Becklin, E. E., Wynn-Williams, C. G., & Harper, D. A. 1984, ApJ, 282, 427
Telesco, C. M., & Harper, D. A. 1980, ApJ, 235, 392
Thronson, H. A., et al. 1989, ApJ, 343, 158
Tully, R. B. 1988, Nearby Galaxies Catalog (New York: Cambridge University Press)
Unger, S. W., Pedlar, A., Axon, D. J., & Whittle, M. 1987, MNRAS, 228, 671
Wilson, A. S., & Heckman, T. M. 1985, in Astrophysics of Active Galaxies and Quasi-Stellar Objects, ed. J. S. Miller (Mill Valley, CA: University Science Books), p. 39
Wilson, A. S., & Ulvestad, J. E. 1983, ApJ, 275, 8
Wilson, A. S., Ward, M. J., & Haniff, C. A. 1988, ApJ, 334, 121